DOI: 10.13009/EUCASS2017-369

7TH EUROPEAN CONFERENCE FOR AERONAUTICS AND AEROSPACE SCIENCES (EUCASS)

DOI:

Response of a Transcritical Coaxial Flame to Fuel Injection Rate Modulations: Analysis and Low-Order Modeling of the Generation of Unsteady Heat Release Rate

Robin Nez[1,2,†], *Thomas Schmitt*[1], *Manuel Gonzalez-Flesca*[1,2], *Sébastien Candel* [1] *and Sébastien Ducruix* [1]
[1]*Laboratoire EM2C, CNRS, CentraleSupélec, Université Paris-Saclay*
Grande Voie des Vignes 92295 Châtenay-Malabry, France
[2]*CNES DLA*
52 rue Jacques Hillairet 75612 Paris Cedex France
[†]Corresponding author: robin.nez@centralesupelec.fr

Abstract

Acoustic pressure fluctuations within the combustion chamber or the plenums of a liquid-rocket engine can induce temporal modulations of the propellants injection velocities. The dynamic response of a transcritical coaxial flame to such velocity modulations is here investigated as it is thought to be one of the mechanisms that can promote high-frequency combustion instabilities. A low-order model for this process is proposed, assuming that the modulation induces fluctuating flame stretch rates traveling along the flame front. This question is then addressed through Large-Eddy Simulation (LES). The annular fuel stream of a single element LOx/GCH_4 injector is acoustically modulated at several frequencies. The proposed model is in reasonable agreement with the flame response extracted from the LES in terms of both gain and phase.

1. Introduction

High-Frequency (HF) combustion instabilities have always constituted an important source of failure for liquid propellant propulsion systems. Today it is still one of the main challenges for the development of a Liquid Rocket Engine (LRE), see among others the review by Oefelein and Yang.[16] These instabilities are due to a resonant coupling that can occur between acoustics, hydrodynamics and combustion, see Culick,[7] Yang and Anderson.[1] Under certain conditions, this coupling can constitute a closed-loop dynamical system which can then lead to self-sustained pressure oscillations. It is of prime importance to predict these unstable operating conditions and for that purpose to develop engineering modeling tools to decrease the need for hot-fire tests and reduce engine development costs. Large-Eddy Simulation (LES) constitutes a promising approach (see Hakim *et al.*[9] and Urbano *et al.*[31]), but currently available computational resources make it too expensive to be used as a design tool in the space propulsion industry. Much effort is consequently put into the development of low-order modeling tools (Candel *et al.*,[3] Pieringer *et al.*,[18] Schulze and Sattelmayer[26]). These tools are designed to perform stability analyses or to predict limit cycle oscillations at the expense of a reduced computational demand. However, they require submodels to account for the dynamic response of the flames to the acoustic or hydrodynamic perturbations and then require a significant modeling effort. As many flame response models are required as there are thermoacoustic coupling mechanisms at play in the engine. One possible coupling mechanism can be the consequence of the fluctuating injection velocity of one of the propellants. Pressure oscillations within the combustion chamber and/or the injection manifolds can indeed modulate the pressure drop across an injector element and consequently excite the flame. This has already been observed within lab-scale experiments, see for instance the observations reported by Noiray *et al.*[15] As experimental diagnostics are usually limited by the extreme conditions prevailing in configurations typical of LREs, LES is increasingly used to study flame dynamics and to provide validation data to low-order models. The dynamics of a transcritical coaxial flame under transverse acoustic forcing were for example simulated by Hakim *et al.*[10] The objective is here to propose a model for the heat release rate of a fuel-modulated transcritical coaxial flame and to carry out simulations for validation. the purpose of such a submodel would be to be implemented in a stability analysis tool. In section 2, a possible coupling mechanism between hydrodynamics and heat release rate is suggested and a model for the flame response is derived. In section 3, an extensive database of numerical results for modulated transcritical flames is constituted and the flame response is characterized. In section 4 the model predictions are confronted to the LES database for validation.

DOI: 10.13009/EUCASS2017-369

2. Low order modeling

The problem considered in this article is represented schematically in Figure 1. A coaxial injector feeds transcritical oxygen and gaseous methane and establishes a flame that is stabilized in the close vicinity of the lips of the LOx injection tube. The fuel stream is modulated around its mean value. The modulation of the fuel stream produces velocity disturbances within the annular jet which then propagate along the reactive region. These velocity perturbations translate into flame stretch rate disturbances, which in turn can induce fluctuating heat release rates. The flame stretch rate is defined as the velocity field divergence in directions tangential to the flame sheet (see Poinsot and Veynante[19]):

$$\epsilon = \nabla_t \cdot \mathbf{u}_t, \tag{1}$$

where the subscript t refers to the tangential component of ∇ operator and $\mathbf{u}_t$ is the tangential component of the velocity field with respect to the flame front. This local tangential plane can be defined as the plane which, at each spatial location, is orthogonal to the gradient of any transported scalar, for instance mixture fraction, a species mass fraction, or temperature.

2.1 Vortical perturbation propagation

The shed velocity disturbances are associated with a vorticity mode. They are then characterized by a phase velocity of convective nature. As a first approximation, we assume that this phase velocity is equal to the annular injector bulk velocity u_e. This propagation at u_e is qualitatively depicted in Figure 1.

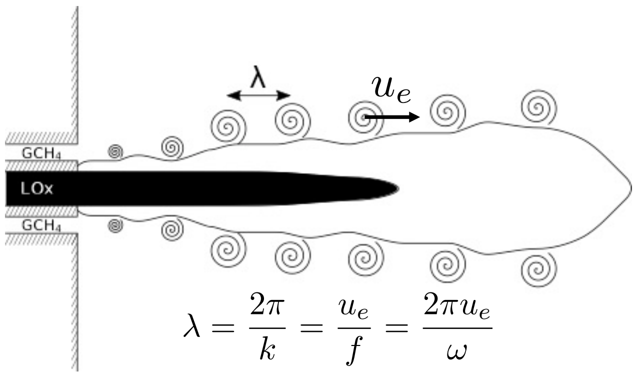

Figure 1: Schematic depicting the effect of the modulation on the flow.

It is reasonable to assume at this stage that the problem is essentially one-dimensional. This is admittedly not quite right but constitutes a good approximation because the flame expansion is relatively slow. This is justified by recalling that cryogenic flames typically encountered in liquid rocket engines are characterized by large outer to inner momentum flux ratios, typically of the order of 10 or higher. This feature, and the significant stratification between the dense inner cryogenic jet and the light annular stream, lead to the production of flames with fairly small opening angles. Now, the traveling velocity perturbation may be assumed to be monochromatic and may be written in the standard form:

$$u(x,t) = u_e(1 + a\sin(\omega t - \kappa x)), \tag{2}$$

where u_e is the local mean velocity, a designates the relative amplitude of the perturbations, $\omega = 2\pi f$ represents the angular frequency related to the modulation and $\kappa = \omega/u_e$ is the wavenumber. The wavenumber is here real and constant as the simplified disturbed velocity signal that we have chosen is characterized by a constant amplitude a and a constant phase velocity u_e.

2.2 Local response of the flame

Small perturbations are assumed. We then start by expanding variables to first order:

DOI: 10.13009/EUCASS2017-369

$$\begin{aligned} u(x,t) &= u_e + u'(x,t), \\ \epsilon(x,t) &= \epsilon_0(x) + \epsilon'(x,t), \\ \dot{q}(x,t) &= \dot{q}_0(x) + \dot{q}'(x,t), \end{aligned} \tag{3}$$

where the subscript 0 denotes a temporal average and $'$ a perturbation around the average. Here $\dot{q}$ is the surface heat release rate and ϵ the flame stretch rate. Considering our one-dimensional flame, with x the axial coordinate, the modulated strain rate $\tilde{\epsilon}'(x,t)$ imposed by the velocity modulation is given by:

$$\tilde{\epsilon}'(x,t) = \nabla_t \cdot \mathbf{u'}_t(x,t) = \frac{\partial u'(x,t)}{\partial x}. \tag{4}$$

The assumed monochromatic velocity distribution along the flame then yields:

$$\tilde{\epsilon}'(x,t) = -u_e a \kappa \cos(\omega t - \kappa x). \tag{5}$$

The change in surface heat release rate related to a flame stretch rate disturbance can be thought of as the consequence of a contraction or expansion of species concentrations and temperature fields and hence of the resulting modification of diffusive fluxes. There is however a time delay characterizing this conversion of hydrodynamic stretching into enhanced scalar diffusion across the shear layer, which results from the coupled multi-species Navier-Stokes equations. The instantaneous heat release rate response of an unsteady flame then depends on the entire time history of the stretch rate field. Haworth *et al.*[11] considered the problem of a counter-flow diffusion flame and solved the problem analytically. They demonstrated that, in the infinitely fast chemistry limit, a modulated one-dimensional diffusion flame burns with an effective flame stretch rate $\epsilon(x,t)$ - *i.e.* the stretch rate that would give the stationary flame the same heat release rate - which depends on the actual flame stretch rate $\tilde{\epsilon}(x,t)$ by verifying the following differential equation:

$$\frac{d\epsilon(x,t)}{dt} = -2\epsilon(x,t)^2 + 2\epsilon(x,t)\tilde{\epsilon}(x,t). \tag{6}$$

This temporal response of the effective flame stretch rate actually constitutes a second-order low-pass filter. By substituting for the actual flame stretch rate signal $\tilde{\epsilon}(x,t)$ from Eq. 5 and integrating one can express the effective flame stretch rate disturbance field as shown by Candel:[2]

$$\epsilon'(x,t) = -\frac{u_e a \kappa}{1 + (\omega/(2\epsilon_0))^2}\left(\cos(\omega t - \kappa x) + \frac{\omega}{2\epsilon_0}\sin(\omega t - \kappa x)\right), \tag{7}$$

We now need to express the temporal response of heat release rate to a time varying flame stretch rate. Under a fast chemistry assumption and for a steady flame, heat release rate is a linear function of the square root of flame stretch rate (see for instance Pons *et al.*[21]):

$$\dot{q}(x) \propto \epsilon(x)^{1/2}. \tag{8}$$

Assuming small fluctuations $\epsilon'(x,t)$ around $\epsilon_0(x)$, one obtains:

$$\frac{\dot{q}'(x,t)}{\dot{q}_0(x)} = \frac{\epsilon'(x,t)}{2\epsilon_0(x)}. \tag{9}$$

By injecting Eq. 9 into Eq. 7, the space-time response of the flame in terms of surface heat release rate as a function of the modulated velocity signal takes the form:

$$\frac{\dot{q}'(x,t)}{\dot{q}_0(x)} = -\frac{u_e a \kappa}{2\epsilon_0}\frac{1}{1 + (\omega/(2\epsilon_0))^2}\left(\cos(\omega t - \kappa x) + \frac{\omega}{2\epsilon_0}\sin(\omega t - \kappa x)\right). \tag{10}$$

DOI: 10.13009/EUCASS2017-369

If the axial distribution of mean heat release rate $\dot{q}_0(x)$ is known, for example from a numerical simulation, Eq. 10 can be integrated over the whole flame - *i.e.* to a distance where $\dot{q}_0(x)$ drops to zero - to determine the global heat release rate perturbation and deduce the corresponding relative level of fluctuation:

$$\frac{\dot{Q}'(t)}{\dot{Q}_0} = -\frac{u_e a \kappa}{2\epsilon_0 \dot{Q}_0} \int \frac{\dot{q}_0(x)}{1 + (\omega/(2\epsilon_0))^2} \left(\cos(\omega t - \kappa x) + \frac{\omega}{2\epsilon_0} \sin(\omega t - \kappa x) \right) dx, \tag{11}$$

where $\dot{q}_0(x)$ is the average heat release rate deduced from a simulation, $\dot{Q}'(t)$ is the total heat release rate fluctuation and $\dot{Q}_0$ the total average heat release rate. The only remaining unknown is the average stretch rate ϵ_0. Strictly speaking, $\dot{Q}_0$ and $\dot{Q}'(t)$ are heat release rates per unit circumferential length. However, considering our simplified 1D model we can arbitrarily substitute surface quantities $\dot{q}$ with heat release rates per unit length in the x-direction, so that after integrating $\dot{Q}_0$ and $\dot{Q}'(t)$ actually represent total heat release rates.

2.3 Canonical application: case of a uniform mean flame

It is interesting to introduce a further simplification of the previously defined flame model, which in its present form necessitates *a priori* knowledge of the mean axial distribution of heat release rate $\dot{q}_0(x)$ within the flame. The mean heat release rate is approximated by a rectangular function depicted in Figure 2.

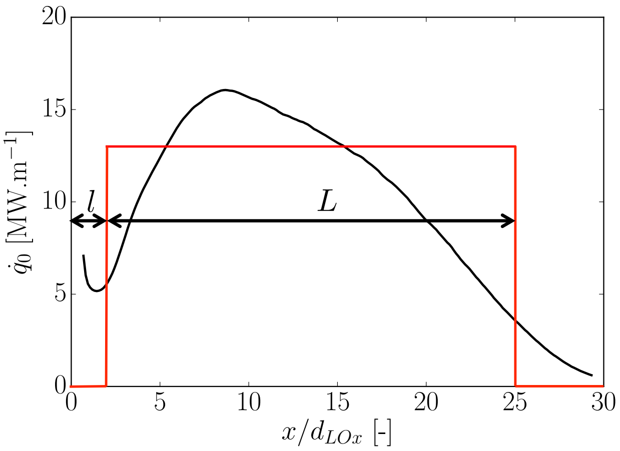

Figure 2: Mean heat release rate may be approximated in the form of a rectangular function. Black: LES profile. Red: 'equivalent flame'.

The heat release rate is now assumed to be constant over an effective length L which would be shifted by a distance l from the injection plane in order to account for the low heat release rates encountered over the first few millimeters:

$$\dot{q}_0(x) = \begin{cases} \dfrac{\dot{Q}_0}{L} & \text{for } x \in [l\ ;\ l+L], \\ 0 & \text{otherwise.} \end{cases} \tag{12}$$

The flame-integrated heat release rate fluctuation is then given by:

$$\frac{\dot{Q}'(t)}{\dot{Q}_0} = -\frac{u_e a}{\epsilon_0 L} \frac{\sin\left(\frac{\kappa L}{2}\right)}{1 + (\omega/(2\epsilon_0))^2} \left(\cos(\omega t - \frac{\kappa L}{2} - \kappa l) + \frac{\omega}{2\epsilon_0} \sin(\omega t - \frac{\kappa L}{2} - \kappa l) \right). \tag{13}$$

In frequency domain this corresponds to the following transfer function between total heat release rate disturbance and velocity disturbance at the injector exit:

$$F(\omega) = \frac{\widehat{\dot{Q}'}(\omega)/\dot{Q}_0}{\widehat{u'_e}(\omega)/u_e} = \frac{u_e \sin\left(\frac{\kappa L}{2}\right)}{\epsilon_0 L} \frac{\exp\left(-j\,(\kappa L/2 + \kappa l + \pi/2 + \theta)\right)}{\left(1 + \left(\frac{\omega}{2\epsilon_0}\right)^2\right)^{1/2}}, \tag{14}$$

with $\theta = \tan^{-1}(\omega/(2\epsilon_0))$.

DOI: 10.13009/EUCASS2017-369

2.4 Analysis of the physical implications of the model

In addition to circumventing the need for *a priori* knowledge of the flame structure, this simplified version of the model has the advantage to help the physical understanding of the underlying mechanism. Three main parameters characterize the model response, and their physical meaning and practical effects can be explained by representing the model transfer function Eq. 14 through Bode diagrams (Figure 3).

- The gain diagram displays a decaying envelope. This behavior is related to the low-pass filter nature of the link between actual flame stretch rate and heat release rate exposed previously. This second-order low-pass filter can be clearly identified in Eq. 14 as the quotient $u_e / \left(\epsilon_0 L \left(1 + \left(\frac{\omega}{2\epsilon_0} \right)^2 \right)^{1/2} \right)$. It is characterized by its cutoff frequency $f_c = \epsilon_0/\pi$. Practically, ϵ_0 then essentially drives the response amplitude at frequencies close to f_c.
- The lobes-shaped gain diagram from Figure 3 indicates that the low-pass behavior of the modeled mechanism is superimposed with a tendency to oscillate in frequency domain. This corresponds to the presence in the transfer function of the factor: $\sin\left(\frac{\kappa L}{2}\right)$. This reflects the non-compactness of the flame with respect to the propagating velocity disturbances. These hydrodynamic disturbances are non-compact as their wavelengths are shorter than the flame length: $\lambda < L$. One can then define the - real valued - number of flow disturbances present within the reactive region at each time:

$$N_d = \frac{L}{\lambda}. \tag{15}$$

  In the case where N_d ends up being an integer, the summation of every wavelength contribution will be null. If it is real valued, the incomplete wavelength present within the reactive region will constitute the disturbance in heat release rate. L drives the lobes width in frequency domain, this width being the inverse of the residence time within the reactive region. This residence time, and thus L, also drives the slope of the phase diagram.
- The length l does no appear in terms affecting the gain, but shares a role similar to L in terms of phase: it constitutes an additional time-lag: $t_d = (L/2 + l)/u_e$ is the effective time-lag of the total heat release rate response to the modulation.

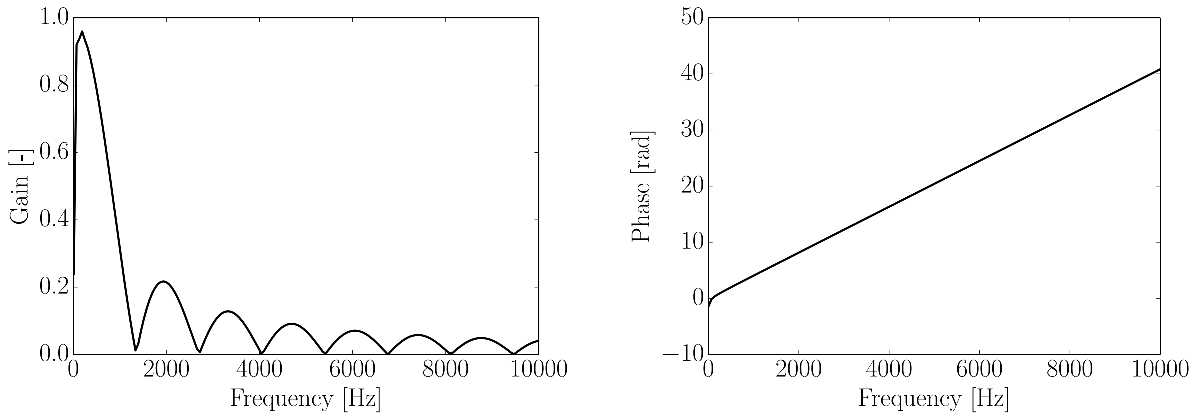

Figure 3: Bode diagrams resulting from the low order model.

It is now logical to see if this model matches what can be deduced from numerical simulations.

3. Large eddy simulations

3.1 Numerical setup

The setup corresponds to the configuration studied by Hakim *et al.*[10] The domain consists in an almost cubic chamber, equipped with a single shear coaxial element on one end and a small exhaust pipe on the other. The main dimensions of

DOI: 10.13009/EUCASS2017-369

the chamber are given in Figure 4a. The dimensions of the shear coaxial injector are quoted in Figure 4b. The injector dimensions can be compared to those found in the G2 experimental setup studied by Singla *et al.*[28] on the Mascotte test rig from Onera, which was itself designed to reproduce conditions typical of actual engines. It can nonetheless be noted that in the present configuration the dimensions of the chamber are large compared to those of the injector element. This is to avoid any confinement effect on the flow dynamics in order to facilitate the analysis of the phenomena of interest. Another substantial specificity of the present geometric setup compared to the aforementioned experiment or real engine injectors is that the LOx post is not tapered. This is to allow for coarser mesh resolutions in the vicinity of the injector, thus facilitating extensive parametric investigations.

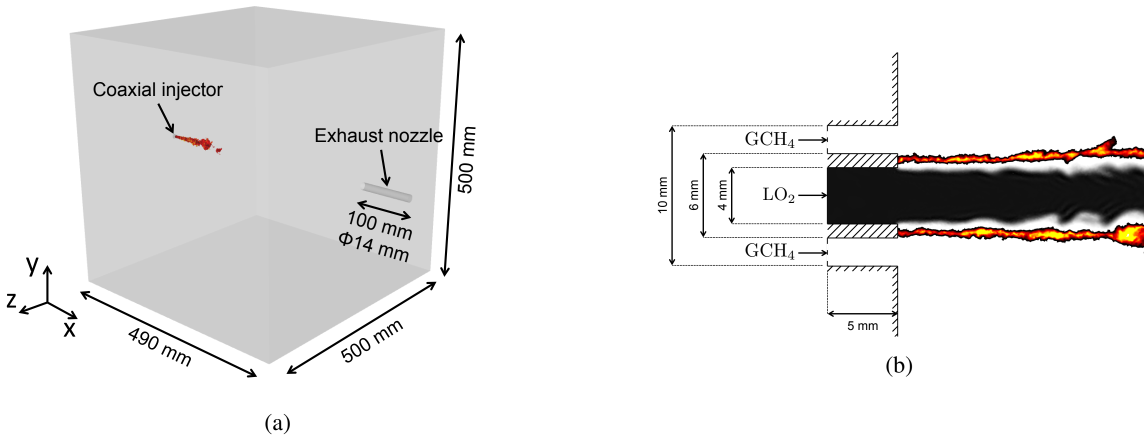

Figure 4: Depiction of the computational domain and dimensions of the injector.

The mean chamber pressure is stabilized to 1.17×10^7 Pa. This is well above the critical pressures of methane as well as oxygen and Hakim *et al.*[10] demonstrated that, depending on the mixture fraction, the burnt mixture can either be supercritical or in a gaseous state (subcritical pressure but supercritical temperature). No two-phase flow regime can then be encountered in this configuration. The details of the injection parameters are given in Table 1. The mixture ratio E and the momentum flux ratio J are defined as follows:

$$\mathrm{E} = \frac{\dot{m}_{\mathrm{O_2}}}{\dot{m}_{\mathrm{CH_4}}}, \tag{16}$$

$$\mathrm{J} = \frac{\rho^0_{\mathrm{CH_4}} (u^0_{\mathrm{CH_4}})^2}{\rho^0_{\mathrm{O_2}} (u^0_{\mathrm{O_2}})^2}. \tag{17}$$

The values of these parameters are quite similar to those of the C-60 configuration studied in the Mascotte test rig and further details can be found in Juniper *et al.*[12]

Table 1: Load points describing parameters.
⋆ : low annular velocity load point.
† : high annular velocity load point.

LOx post		GCH_4 post		Global parameters	
$\dot{m}_{\mathrm{O_2}}$ [g.s^{-1}]	141	$\dot{m}_{\mathrm{CH_4}}$ [g.s^{-1}]	$430^\star$ or $860^\dagger$	p_c [MPa]	11.7
$T^0_{\mathrm{O_2}}$ [K]	100	$T^0_{\mathrm{CH_4}}$ [K]	300	E [-]	$0.328^\star$ or $0.164^\dagger$
$\rho^0_{\mathrm{O_2}}$ [kg.m^{-3}]	1122	$\rho^0_{\mathrm{CH_4}}$ [kg.m^{-3}]	88	J [-]	$7.41^\star$ or $29.6^\dagger$
$u^0_{\mathrm{O_2}}$ [m.s^{-1}]	10.0	$u^0_{\mathrm{CH_4}}$ [m.s^{-1}]	$97.2^\star$ or $194.4^\dagger$		
$Re_{\mathrm{O_2}}$ [-]	2.60×10^5	$Re_{\mathrm{CH_4}}$ [-]	$2.74 \times 10^{6\star}$ or $5.48 \times 10^{6\dagger}$		

The annular GCH_4 stream is modulated by prescribing a sinusoidal incoming acoustic perturbation at the stream's inlet boundary. The amplitude of the prescribed acoustic velocity signal is about 10% of the annular bulk velocity *i.e.* 10 m.s^{-1} or 20 m.s^{-1} depending on the load point. The simulated modulated operating conditions are gathered in Table 2.

DOI: 10.13009/EUCASS2017-369

A red cross denotes an operating point that was not treated to manage available computational resources. Reference simulations with no modulation have been performed so that the effects of the modulation can be easily assessed.

Table 2: List of modulated operating points.

Injection conditions			Modulation frequencies [Hz]					
$u^0_{CH_4}$ [m.s^{-1}]	E [-]	J [-]	500	1000	2000	3500	5000	8000
97.2	0.328	7.41	✔	✔	✔	✔	✔	✔
194.4	0.164	29.6	✗	✔	✔	✔	✔	✔

3.2 Flow solver

The present Large Eddy Simulations are carried out using the flow solver AVBP developed at Cerfacs and IFPEN. It is used to integrate the filtered three-dimensional compressible Navier-Stokes equations for reacting multispecies mixtures on unstructured meshes (Schönfeld and Rudgyard,[25] Gourdain *et al.*[8]). The discretization employs a Two-Step Taylor-Galerkin scheme (TTGC) which is third order in space and time (Colin and Rudgyard[5]). Characteristic boundary conditions (Thompson,[30] Poinsot and Lele[20]) are employed to allow the acoustic forcing of the computational domain, as well as to control the amount of acoustic energy entering and leaving the domain, see Selle *et al.*[27] AVBP's real-gas extension (Pons *et al.*,[22] Schmitt *et al.*[23,24]) employed in the present calculations and developed at EM2C and Cerfacs takes into account thermodynamic non-idealities through the use of cubic equations of state, the Soave-Redlich-Kwong (SRK) equation being employed here (Soave[29]). The real-gas transport properties are represented by making use of Chung's laws (Chung *et al.*[4]). Numerical schemes and characteristic boundary conditions are adapted to comply with the real-gas thermodynamics. Subgrid-scale momentum fluxes are modeled by the Wall Adapting Large Eddy (WALE) model (Nicoud and Ducros[14]) as it is well-suited for shear flows, its eddy-viscosity vanishing in purely strained regions of the flow. Subgrid-scale energy and species fluxes are approximated by constant turbulent Prandtl and Schmidt numbers $Pr_t = Sc_t = 0.75$. Chemical conversion is represented with the infinitely fast chemistry model IFCM described in Schmitt *et al.*[23] It was shown by Pons *et al.*[21] that, for stretched counter-flow high pressure methane-oxygen flames, chemical times defined as the inverse of the extinction strain rates are always several orders of magnitude below the characteristic mixing and acoustic times related to the present numerical configuration. Equilibrium mass fractions are then tabulated in terms of the mixture fraction and its variance which are both transported, and the following species are retained in order to properly estimate the equilibrium burnt gases temperature at any mixture fraction: CH_4, O_2, CO_2, H_2O, CO and H_2. The species source terms are then computed according to the procedure detailed by Schmitt *et al.*[23] Injector walls are treated as Neumann boundary conditions through the enforcement of wall stresses deduced from a mixed law of the wall (typical logarithmic law or linear law depending on the local mesh resolution). Synthetic anisotropic turbulence is injected at the domain inlets by enforcing mean and RMS profiles for each velocity component as well as for deviatoric Reynolds stresses. These profiles result from the LES of a periodic pipe flow setup with similar Reynolds number and grid resolution. This synthetic turbulence field is defined by constructing of set of solenoidal modes employing the method from Kraichnan and Celik,[13] so that no acoustic noise is produced. This set of modes ends up constituting a Passot-Pouquet spectrum.[17] The tetrahedral mesh employed counts 2.5×10^6 vertices (14.5×10^6 elements). It is refined within the highly stratified region around the dense oxygen jet, with the finer resolution corresponding to 7 elements per injector lip thickness and 25 elements per LOx post diameter and gradually coarsened further downstream.

3.3 Results and analysis

For the sake of clarity, comparison of only some of the simulations is performed here. The set of points selected allows an adequate analysis of the model defined previously. This set includes the following modulated operating points: 1000 Hz, 2000 Hz, 5000 Hz and 8000 Hz with $u^0_{CH_4} = 97.2$ [m.s^{-1}], as well as the corresponding modulation-free simulation. However, all simulated operating points will serve to compare the proposed flame response model.

3.3.1 Instantaneous flow visualizations

The main characteristics of the reactive coaxial jet flows resulting from both modulated and non-modulated computations are illustrated by instantaneous snapshots in Figure 5. The red iso-contour of oxygen mass fraction is here

DOI: 10.13009/EUCASS2017-369

employed as a tracker of the flame front. The inner dense jet gets corrugated, the strong density gradients then rapidly decaying downstream due to the enhanced mixing. The inner jet also tends to shed dense oxygen pockets in an intermittent fashion. As justified in the previous section through the derivation of the flame response model, the light annular jet opening is quite low for this kind of setup, and the oxygen mass fraction iso-line demonstrates that the reactive region remains close to the inner oxygen core. Examination of the modulated cases snapshots motivates the division of these operating points into two groups. On the one hand, cases modulated at 1000 Hz and 2000 Hz do not significantly depart from the previous description of the non-modulated flow dynamics. On the other hand, modulations at 5000 Hz and 8000 Hz significantly affect the dynamics of the flow. At these frequencies, the shed vorticity disturbances are much shorter and enhance flame wrinkling when they are convected downstream. These shorter vortical structures tend to cause the early destabilization of both streams, one consequence being a drastically shortened dense inner core. Time-averaged results actually demonstrate that characteristic lengths of the flame are strongly reduced as well. Due to the more intense viscous dissipation resulting from their shorter scales, these energetic coherent structures rapidly decay, and even disappear within fully developed turbulence scales even before flowing past the flame tip.

3.3.2 Characterization through first and second order statistical moments

The aforementioned varying destabilization length of the inner oxygen jet can be evaluated in detail through Figure 6. While the 1000 Hz operating point almost perfectly matches the non-modulated computation in terms of mean axial velocity, increasing the modulation frequency gradually shifts the accelerating region upstream. This steep velocity increase corresponds to the end of the intact oxygen core, where high-velocity gases are free to flow inward to the jet axis. The spatial evolutions of resolved turbulent kinetic energy support the explanation suggested earlier: the curves extracted from higher frequency (5000 and 8000 Hz) cases indicate that the inner jet is destabilized at about 5 LOx post diameters from the injection plane, compared to about 10 at lower frequencies (1000 and 2000 Hz) and in the unmodulated case. Mean and RMS density plots are shown in Figure 7 and again illustrate the shortening of the dense core at higher frequencies, while fields of oxygen mass fraction and temperature demonstrate that the statistical structure of the flame is not really altered, apart from being shifted upstream. Before tackling the question of the heat release rate response, it is worth examining its mean spatial distribution for each frequency of modulation. For that sake, the time-averaged heat release rate is integrated over thin slices extending over the full domain in the transverse directions. The resulting data is plotted in Figure 8. Here the difference in behavior between lower and higher frequency operating points is striking. Although the decay in heat release rate beyond 10 LOx post diameters does not differ significantly from case to case, the high-frequency cases involving the generation of shorter coherent structures displays a sharp peak close to the injection plate, where these vortices are more energetic whereas they will be rapidly damped downstream.

3.3.3 Spectral analyses

Some of the numerical probes positions available are shown in Figure 9. Examining the Power Spectral Density (PSD) of velocity signals recorded in the annular destabilizing jet (probe P1b) gives additional insight into the jet dynamics, see Figure 10. The signature of the modulation is always visible, the modulation frequencies being revealed by vertical dashed lines. It is especially interesting to point out the gradual increase of the response amplitude with the forcing frequency for the radial velocity component, whereas it remains fairly constant for every modulation frequency for the axial component. This illustrates again the production of shorter coherent structures at higher forcing frequencies evoked earlier. Additionally, high-frequency harmonics are revealed for 5000 Hz and 8000 Hz operating points. It also appears that higher-frequency modulations spread broad-band energy over the entire spectrum. This may be explained by the corresponding gradual decrease of the difference between the jet natural frequency and the modulation frequency. The annular jet Strouhal number $\mathrm{St} = f h_{\mathrm{CH_4}} / \mathrm{u}_e$, with $h_{\mathrm{CH_4}}$ the annular channel thickness, is then given as an additional abscissa in Figure 10. The unmodulated simulation displays a dominant response of the annular jet for St = 0.36, which appears to be close to the typical value of 0.3 measured for round gaseous jets by Crow and Champagne.[6] The spectrum obtained from the other unmodulated simulation with a doubled methane injection velocity, not shown here, yields the same natural Strouhal number. The same data from probe P2e is plotted in Figure 11. The probe is located at the mean tip of the dense core (20 LOx post diameters), and is expected to give insight into the oxygen jet dynamics. One finds that the spectral contents of the velocity signals do not differ much at this location. We then conclude that even though the modulation drastically shortens the dense jet, its hydrodynamic behavior remains relatively unaffected. In the framework of combustion instabilities analyses, the heat release rate response of the flame is of prime interest. To this purpose, a PSD of the computational domain-integrated heat release rate is given in Figure 12, together with a coherence spectrum for the correlation between annular injection velocity (probe P1a) and domain-integrated heat release rate. Both illustrate a strong response of the flame to the modulation, regardless of the forcing frequency. The strong signal-to-noise ratio obtained for each case is favorable to the determination of accurate transfer function

DOI: 10.13009/EUCASS2017-369

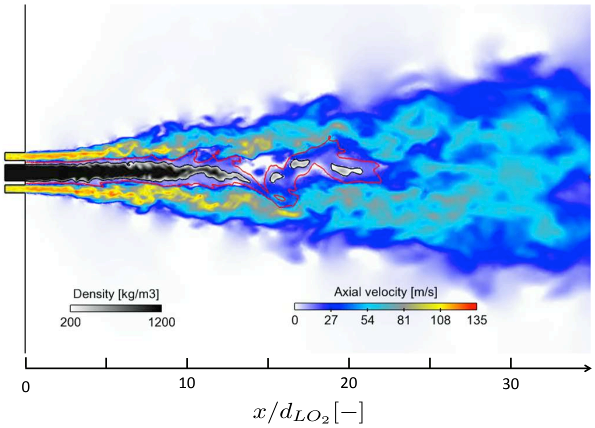

(a) Reference case: no modulation.

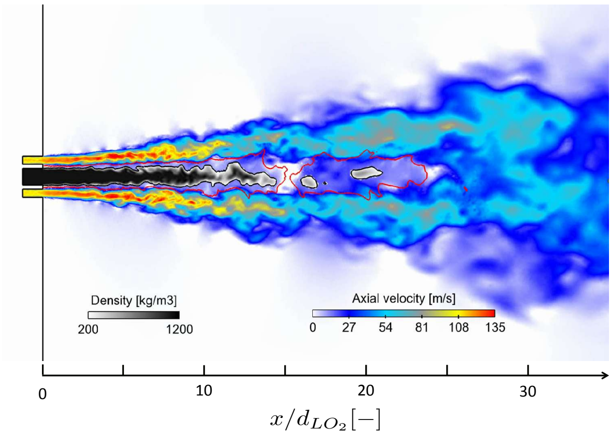

(b) 1000 Hz modulation.

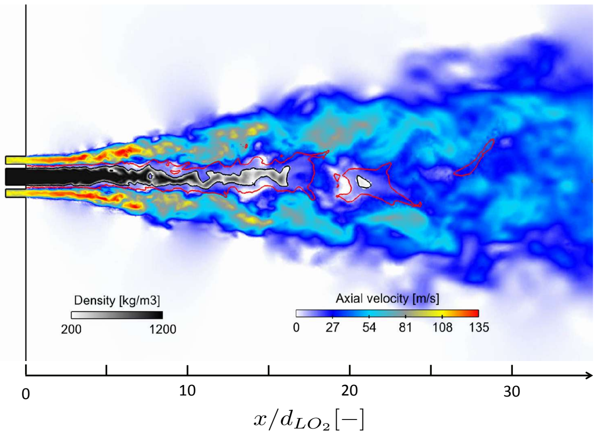

(c) 2000 Hz modulation.

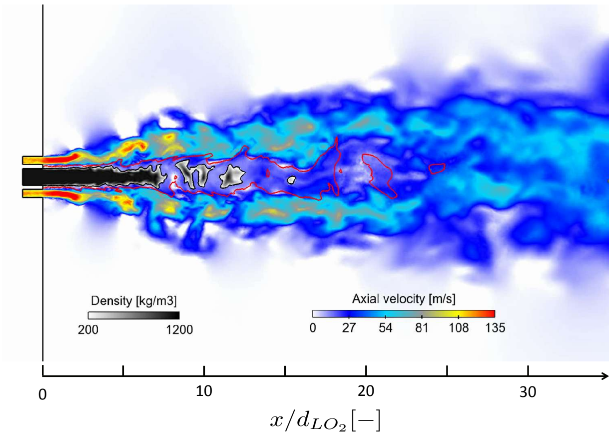

(d) 5000 Hz modulation.

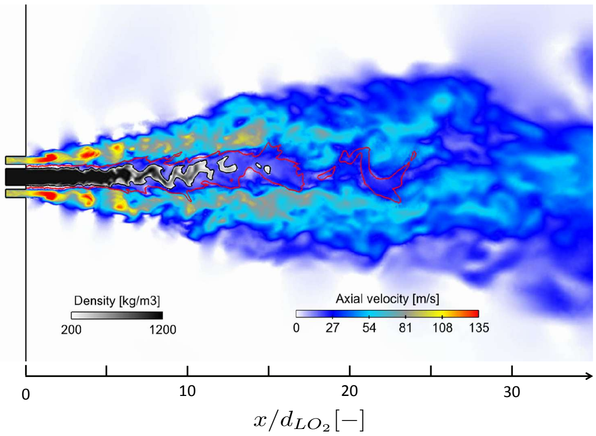

(e) 8000 Hz modulation.

Figure 5: Superimposed instantaneous cuts of axial velocity (white to red) and of density within the dense oxygen jet (gray scale). Red: iso-contour of oxygen mass fraction $Y_{O_2} = 0.5$.

estimates from the LES signals. Some correlations at harmonics of the modulation frequencies are also revealed for the 5000 Hz and 8000 Hz pulsations.

4. Model validation against LES data

Numerical transfer functions between methane injection velocity and total heat release rate can be computed from the LES output signals:

DOI: 10.13009/EUCASS2017-369

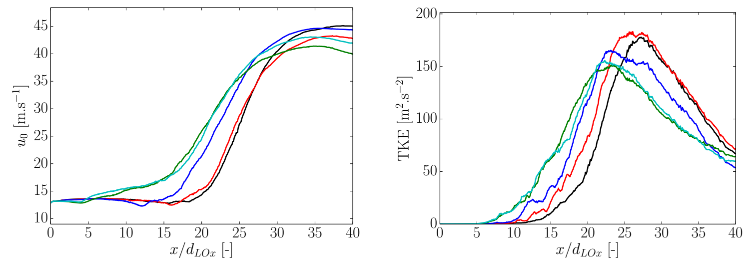

(a) Time-averaged axial velocity. (b) Resolved TKE.

Figure 6: Characterization of the dense oxygen jet dynamics at each modulation frequency through first and second order moments profiles along the jet axis. Black: modulation-free case. Red: f = 1000 Hz. Blue: f = 2000 Hz. Green: f = 5000 Hz. Cyan: f = 8000 Hz.

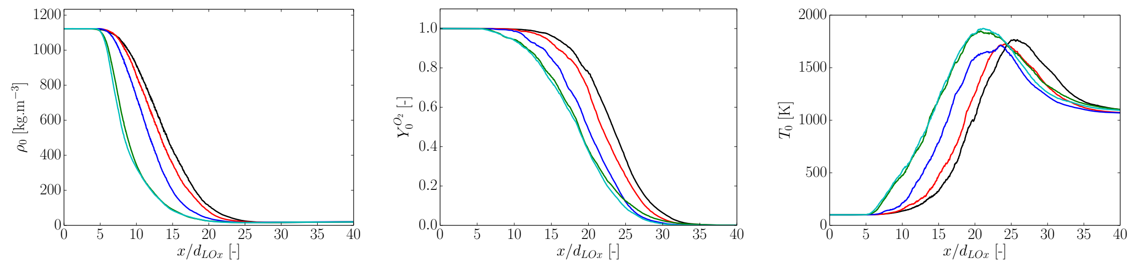

(a) Mean density. (b) Mean oxygen mass fraction. (c) Mean temperature.

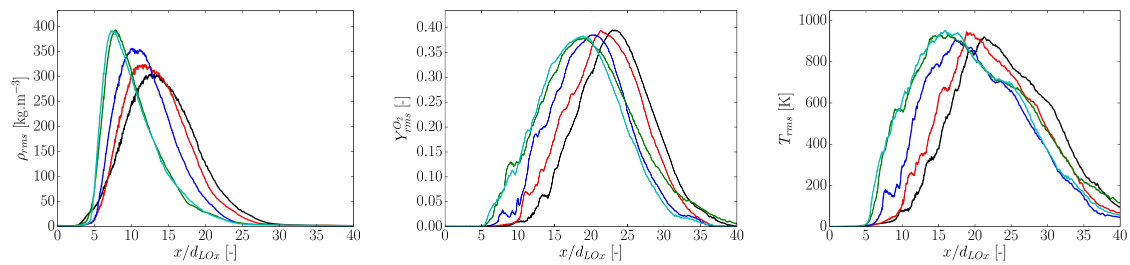

(d) RMS of density. (e) RMS of oxygen mass fraction. (f) RMS of temperature.

Figure 7: Characterization of the flame structure at each modulation frequency through first (top row) and second order moments (bottom row) profiles of scalars along the flame axis. Black: modulation-free case. Red: f = 1000 Hz. Blue: f = 2000 Hz. Green: f = 5000 Hz. Cyan: f = 8000 Hz.

$$F_{LES}(\omega) = \frac{\widehat{S}_{u'\dot{Q}'}(\omega)}{\widehat{S}_{u'u'}(\omega)}, \tag{18}$$

where $\widehat{S}_{u'\dot{Q}'}$ is the cross-power spectrum of u' and $\dot{Q}'$ signals, and $\widehat{S}_{u'u'}$ is the power spectrum of u'. Bode diagrams for all available numerical data points are plotted together with the transfer function deduced from the low order model in Figure 13. The displayed model outputs are obtained for sets of parameters that are given in the caption of the figure.

One observes a fairly good agreement between the model and the LES outputs for both gain and phase and for both load points. The low-pass gain cutoff and the linear evolution of the phase are successfully captured by the model. It is especially encouraging to point out that between the two load points, L is the only parameter that has been adjusted to fit the LES data. This tends to demonstrate the generic validity of the model. In addition, it can be noted that the reduction of L from the 'low-velocity' to the 'high-velocity' load point is consistent with the numerically observed flame shortening resulting from the increased momentum flux ratio. Still, some minor discrepancies for the phase predictions can be seen. In addition, the null response expected at 3500 Hz for the 'high-velocity' load point is not

DOI: 10.13009/EUCASS2017-369

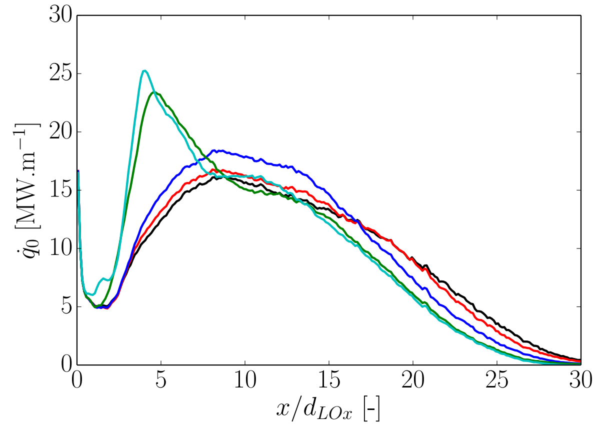

Figure 8: Distribution of the time averaged heat release rate over the flame axis after integration over the transverse directions (y and z) of the domain. Black: modulation-free case. Red: f = 1000 Hz. Blue: f = 2000 Hz. Green: f = 5000 Hz. Cyan: f = 8000 Hz.

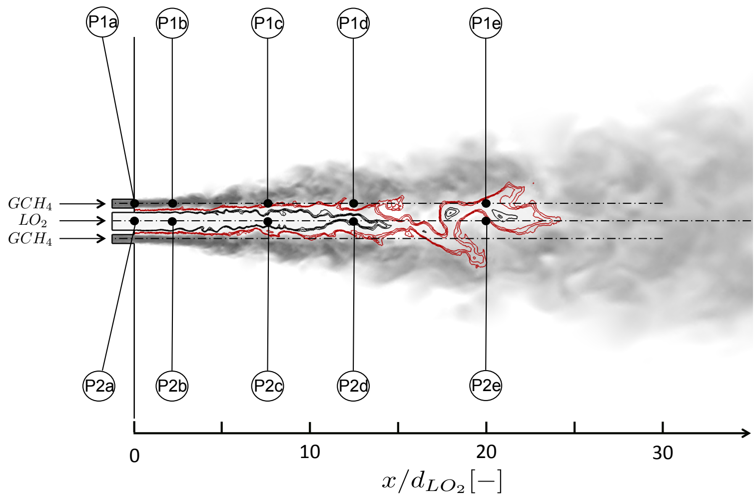

Figure 9: Depiction of the numerial probes locations.

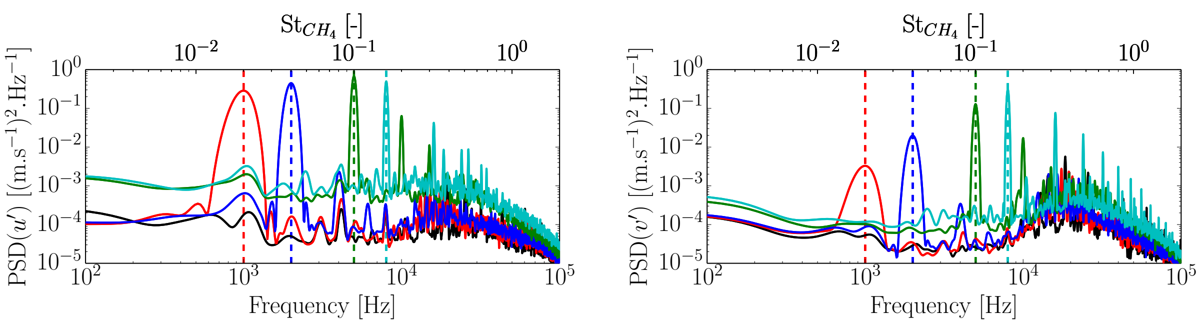

(a) Axial velocity component.

(b) Radial velocity component.

Figure 10: Power spectral densities of velocity components recorded at P1b. Computed using Welch's method, averaging is carried out over 22 blocks using Hann's window, 50% overlapping, zero-padding. The spectral resolution is 205 Hz. Black: modulation-free case. Red: f = 1000 Hz. Blue: f = 2000 Hz. Green: f = 5000 Hz. Cyan: f = 8000 Hz.

observed numerically. These deficiencies can be thought to be related to the mean flame structure dependency with respect to the modulation frequency, which is not taken into account by the model.

DOI: 10.13009/EUCASS2017-369

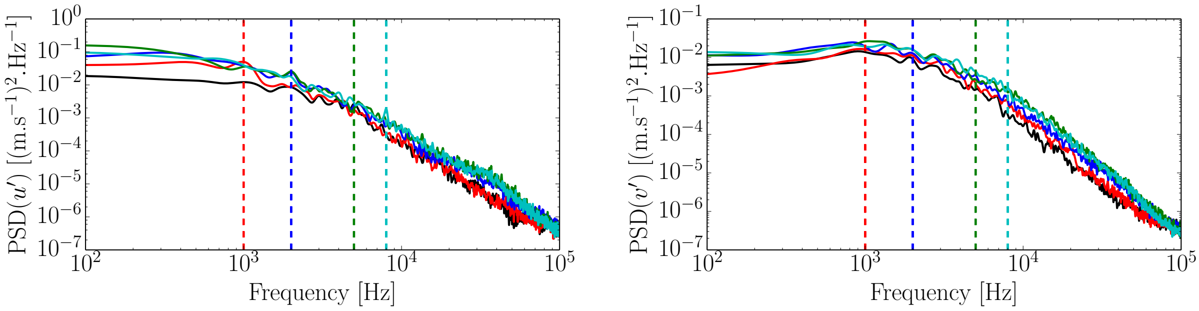

(a) Axial velocity component.

(b) Radial velocity component.

Figure 11: Power spectral densities of velocity components recorded at P2e. Computed using Welch's method, averaging is carried out over 22 blocks using Hann's window, 50% overlapping, zero-padding. The spectral resolution is 205 Hz. Black: modulation-free case. Red: f = 1000 Hz. Blue: f = 2000 Hz. Green: f = 5000 Hz. Cyan: f = 8000 Hz.

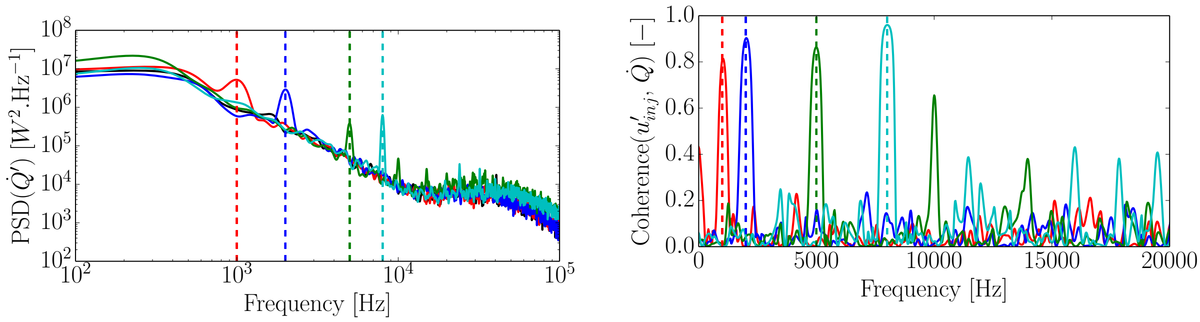

(a) Integrated heat release rate PSD.

(b) Injection velocity - integrated heat release rate coherence spectra.

Figure 12: Spectra computed using Welch's method, averaging is carried out over 22 blocks using Hann's window, 50% overlapping, zero-padding. The spectral resolution is 205 Hz. Black: modulation-free case. Red: f = 1000 Hz. Blue: f = 2000 Hz. Green: f = 5000 Hz. Cyan: f = 8000 Hz.

5. Summary and conclusions

The dynamics of a transcritical coaxial flame is considered in this article. A low-order model representing the unsteady heat release rate produced by a fluctuating fuel injection velocity is derived for small disturbances. It assumes that the modulation of the injection rate produces hydrodynamic disturbances that act on the flame front by inducing fluctuating flame stretch rates. Using a one-dimensional approximation, the perturbed velocity field is modeled by a traveling sine signal. Assuming that chemical times are short compared to the mixing times, the temporal response of the total heat release rate of the flame can be expressed, provided that the mean heat release rate distribution is known. The definition of an 'equivalent flame' through simplification of this mean flame structure into a rectangular function allows to circumvent the need for numerical simulations and to obtain the flame transfer function. Large-Eddy Simulations confirmed the flow dynamics anticipated through the model derivation process. They show the production and convection of vortical structures along the flame front, the flame opening angle remaining low and the flow mainly axial. It is observed that the modulation of the annular stream, though fairly low (10% of the bulk velocity) could significantly alter the mean flow and flame structure beyond a certain critical Strouhal number, in the range [0.04 ; 0.07] in the present setup. The model was finally confronted to the extensive numerical simulation database that had been built and proved to predict the flame response amplitude efficiently. Some small discrepancies are observed in terms of phase predictions, which might be due to the numerically observed frequency-dependent mean flame structure.

DOI: 10.13009/EUCASS2017-369

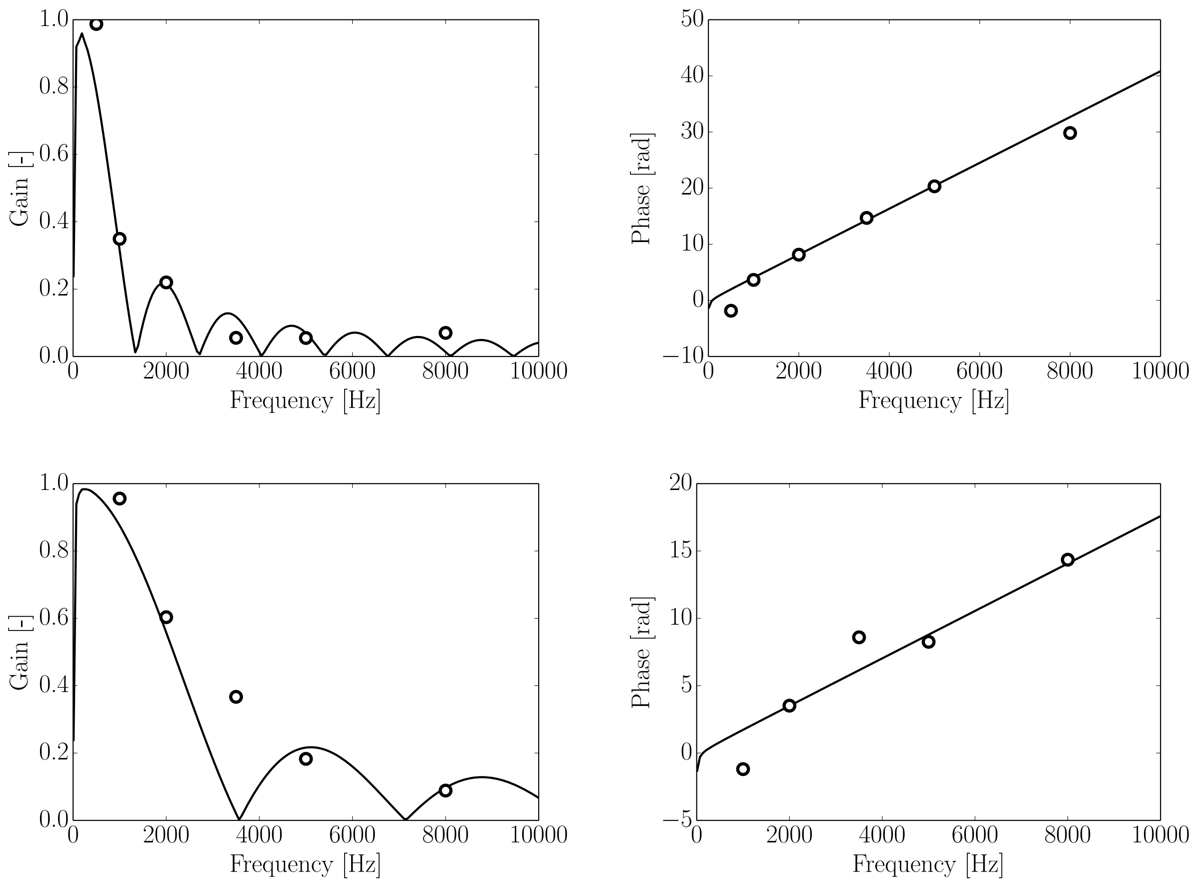

Figure 13: Bode diagrams resulting from the LES (symbols) and from the low order model (continuous line).
First row: 97.2 m.s^{-1} methane bulk velocity. Model inputs: ϵ_0 = 100 s^{-1}, L = 18.5 d_{LOx}, l = 7 d_{LOx}, u_e = 100 m.s^{-1}.
Second row: 194.4 m.s^{-1} methane bulk velocity. Model inputs: ϵ_0 = 100 s^{-1}, L = 14 d_{LOx}, l = 7 d_{LOx}, u_e = 200 m.s^{-1}.

6. Acknowledgments

This work was part of an ongoing PhD thesis which is co-funded by CNES, the French national space agency and Airbus Safran Launchers, the prime contractor for the propulsion systems of the European launcher Ariane 5. It was also carried out in the framework of the French-German initiative REST (Rocket Engine STability). We are thankful to Cerfacs for sharing the solver AVBP with us and for contributing to the development of its real-gas extension. HPC resources of CINES (Centre Informatique National de l'Enseignement Supérieur) were made available by GENCI (Grand Equipement National de Calcul Intensif) through grant x20162b6176.

References

[1] W. Anderson and V. Yang. Liquid rocket engine combustion instability. *Progress in Astronautics and Aeronautics*, 169, 1995.

[2] S. Candel. Combustion dynamics and control: Progress and challenges. *Proceedings of the combustion institute*, 29(1):1–28, 2002.

[3] S. Candel, C. Huynh, and T. Poinsot. Some modeling methods of combustion instabilities. In *Unsteady combustion*, pages 83–112. Springer, 1996.

[4] T. H. Chung, M. Ajlan, L. L. Lee, and K. E. Starling. Generalized multiparameter correlation for nonpolar and polar fluid transport properties. *Industrial & engineering chemistry research*, 27(4):671–679, 1988.

DOI: 10.13009/EUCASS2017-369

[5] O. Colin and M. Rudgyard. Development of high-order taylor–galerkin schemes for les. *Journal of Computational Physics*, 162(2):338–371, 2000.

[6] S. C. Crow and F. H. Champagne. Orderly structure in jet turbulence. *Journal of Fluid Mechanics*, 48(03):547–591, 1971.

[7] F. E. C. Culick. Unsteady motions in combustion chambers for propulsion systems. agardograph. Technical report, NATO/RTO-AG-AVT-039, 2006.

[8] N. Gourdain, L. Gicquel, M. Montagnac, O. Vermorel, M. Gazaix, G. Staffelbach, M. Garcia, J. F. Boussuge, and T. Poinsot. High performance parallel computing of flows in complex geometries: I. methods. *Computational Science & Discovery*, 2(1):015003, 2009.

[9] L. Hakim, A. Ruiz, T. Schmitt, M. Boileau, G. Staffelbach, S. Ducruix, B. Cuenot, and S. Candel. Large eddy simulations of multiple transcritical coaxial flames submitted to a high-frequency transverse acoustic modulation. *Proceedings of the Combustion Institute*, 35(2):1461–1468, 2015.

[10] L. Hakim, T. Schmitt, S. Ducruix, and S. Candel. Dynamics of a transcritical coaxial flame under a high-frequency transverse acoustic forcing: Influence of the modulation frequency on the flame response. *Combustion and Flame*, 162(10):3482–3502, 2015.

[11] D. C. Haworth, M. C. Drake, S. B. Pope, and R. J. Blint. The importance of time-dependent flame structures in stretched laminar flamelet models for turbulent jet diffusion flames. In *Symposium (International) on Combustion*, volume 22, pages 589–597. Elsevier, 1989.

[12] M. Juniper, A. Tripathi, P. Scouflaire, J. C. Rolon, and S. Candel. Structure of cryogenic flames at elevated pressures. *Proceedings of the Combustion Institute*, 28(1):1103–1109, 2000.

[13] R. H. Kraichnan. Diffusion by a random velocity field. *Physics of Fluids (1958-1988)*, 13(1):22–31, 1970.

[14] F. Nicoud and F. Ducros. Subgrid-scale stress modelling based on the square of the velocity gradient tensor. *Flow, Turbulence and Combustion*, 62(3):183–200, 1999.

[15] N. Noiray, D. Durox, T. Schuller, and S. Candel. Mode conversion in acoustically modulated confined jets. *AIAA journal*, 47(9):2053–2062, 2009.

[16] J. C. Oefelein and V. Yang. Comprehensive review of liquid-propellant combustion instabilities in f-1 engines. *Journal of Propulsion and Power*, 9(5):657–677, 1993.

[17] T. Passot and A. Pouquet. Numerical simulation of compressible homogeneous flows in the turbulent regime. *Journal of Fluid Mechanics*, 181:441–466, 1987.

[18] J. Pieringer, T. Sattelmayer, and F. Fassl. Simulation of combustion instabilities in liquid rocket engines with acoustic perturbation equations. *Journal of propulsion and power*, 25(5):1020–1031, 2009.

[19] T. Poinsot and D. Veynante. *Theoretical and numerical combustion*. RT Edwards, Inc., 2005.

[20] T. J. Poinsot and S. K. Lele. Boundary conditions for direct simulations of compressible viscous flows. *Journal of computational physics*, 101(1):104–129, 1992.

[21] L. Pons, N. Darabiha, and S. Candel. Pressure effects on nonpremixed strained flames. *Combustion and Flame*, 152(1):218–229, 2008.

[22] L. Pons, N. Darabiha, S. Candel, T. Schmitt, and B. Cuenot. The structure of multidimensional strained flames under transcritical conditions. *Comptes Rendus Mecanique*, 337(6):517–527, 2009.

[23] T. Schmitt, Y. Méry, M. Boileau, and S. Candel. Large-eddy simulation of oxygen/methane flames under transcritical conditions. *Proceedings of the Combustion Institute*, 33(1):1383–1390, 2011.

[24] T. Schmitt, L. Selle, and B. Ruiz, A .and Cuenot. Large-eddy simulation of supercritical-pressure round jets. *AIAA journal*, 48(9):2133–2144, 2010.

[25] T. Schonfeld and M. Rudgyard. Steady and unsteady flow simulations using the hybrid flow solver avbp. *AIAA journal*, 37(11):1378–1385, 1999.

DOI: 10.13009/EUCASS2017-369

[26] M. Schulze and T. Sattelmayer. Eigenvalue analysis for the prediction of initial growth rates of thermoacoustic instability in rocket motors. In *53rd AIAA Aerospace Sciences Meeting*, page 1606, 2015.

[27] L. Selle, F. Nicoud, and T. Poinsot. Actual impedance of nonreflecting boundary conditions: Implications for computation of resonators. *AIAA journal*, 42(5):958–964, 2004.

[28] G. Singla, P. Scouflaire, J. C. Rolon, and S. Candel. Transcritical oxygen/transcritical or supercritical methane combustion. *Proceedings of the combustion institute*, 30(2):2921–2928, 2005.

[29] G. Soave. Equilibrium constants from a modified redlich-kwong equation of state. *Chemical Engineering Science*, 27(6):1197–1203, 1972.

[30] K. W. Thompson. Time dependent boundary conditions for hyperbolic systems. *Journal of computational physics*, 68(1):1–24, 1987.

[31] A. Urbano, L. Selle, G. Staffelbach, B. Cuenot, T. Schmitt, S. Ducruix, and S. Candel. Exploration of combustion instability triggering using large eddy simulation of a multiple injector liquid rocket engine. *Combustion and Flame*, 169:129–140, 2016.